INTERFACE

royalsocietypublishing.org/journal/rsif

Research

Cite this article: Guasto JS, Estrada JB, Menolascina F, Burton LJ, Patel M, Franck C, Hosoi AE, Zimmer RK, Stocker R. 2020 Flagellar kinematics reveals the role of environment in shaping sperm motility. *J. R. Soc. Interface* **17**: 20200525.
http://dx.doi.org/10.1098/rsif.2020.0525

Received: 3 July 2020
Accepted: 17 August 2020

Subject Category:
Life Sciences–Physics interface

Subject Areas:
biomechanics, biophysics

Keywords:
sperm, flagella, motility, kinematics, taxonomy

Authors for correspondence:
Jeffrey S. Guasto
e-mail: jeffrey.guasto@tufts.edu
Roman Stocker
e-mail: romanstocker@ethz.ch

†These authors contributed equally to this work.

Electronic supplementary material is available online at https://doi.org/10.6084/m9.figshare.c.5111411.

THE ROYAL SOCIETY PUBLISHING

Flagellar kinematics reveals the role of environment in shaping sperm motility

Jeffrey S. Guasto[1], Jonathan B. Estrada[2,3,†], Filippo Menolascina[4,5,†], Lisa J. Burton[6,†], Mohak Patel[3], Christian Franck[3], A. E. Hosoi[6], Richard K. Zimmer[8,9] and Roman Stocker[10,7]

[1]Department of Mechanical Engineering, Tufts University, Medford, MA 02155, USA
[2]Department of Mechanical Engineering, University of Michigan, Ann Arbor, MI 48109, USA
[3]School of Engineering, Brown University, Providence, RI 02912, USA
[4]School of Engineering, Institute for Bioengineering, and [5]Synthsy – Centre for Systems and Synthetic Biology, University of Edinburgh, King's Buildings, EH9 3BF Edinburgh, UK
[6]Department of Mechanical Engineering, and [7]Ralph M. Parsons Laboratory, Department of Civil and Environmental Engineering, MIT, Cambridge, MA 02139, USA
[8]Department of Ecology and Evolutionary Biology, UCLA, Los Angeles, CA 90095, USA
[9]School of Biological Sciences, University of Queensland, St Lucia, Brisbane 4072, Queensland, Australia
[10]Institute of Environmental Engineering, Department of Civil, Environmental and Geomatic Engineering, ETH Zurich, 8093 Zurich, Switzerland

JSG, 0000-0001-8737-8767; JBE, 0000-0003-1083-4597; RS, 0000-0002-3199-0508

Swimming spermatozoa from diverse organisms often have very similar morphologies, yet different motilities as a result of differences in the flagellar waveforms used for propulsion. The origin of these differences has remained largely unknown. Using high-speed video microscopy and mathematical analysis of flagellar shape dynamics, we quantitatively compare sperm flagellar waveforms from marine invertebrates to humans by means of a novel phylokinematic tree. This new approach revealed that genetically dissimilar sperm can exhibit strikingly similar flagellar waveforms and identifies two dominant flagellar waveforms among the deuterostomes studied here, corresponding to internal and external fertilizers. The phylokinematic tree shows marked discordance from the phylogenetic tree, indicating that physical properties of the fluid environment, more than genetic relatedness, act as an important selective pressure in shaping the evolution of sperm motility. More broadly, this work provides a physical axis to complement morphological and genetic studies to understand evolutionary relationships.

1. Introduction

Despite nearly 70 years of research into the hydrodynamics, mechanics and molecular mechanisms of sperm flagellar motility [1–3], a quantitative comparison of sperm swimming kinematics across species has been lacking. Sperm motility is a key trait in sexual reproduction [3–6], enabling the delivery of genetic cargo to distant egg cells for organisms ranging from marine invertebrates [6,7] to mammals [4] and even plants [8]. Determining how sperm motility has evolved to serve this function [9] in a broad range of physical environments [10,11] is fundamental to our understanding of the relationships among species.

Physical environmental factors play an important role in shaping the evolution of flagellar kinematics [9], where external and internal fertilizers experience distinctly different fluid environments [2]. The spermatozoa of external fertilizers often swim in aquatic environments characterized by low, Newtonian viscosity. Under these conditions, numerical simulations of flagellar beating revealed that bending waves of uniform amplitude along the flagellum are the optimal propulsion strategy to maximize swimming efficiency, or equivalently, swimming speed [12]. By contrast, the spermatozoa of internal fertilizers experience a range of fluid environments, such as in cervical mucus, characterized by elevated viscosity and complex rheology, for example, viscoelasticity owing to

suspended biopolymers and proteins [13]. In viscoelastic fluids, numerical simulations have shown that bending waves characterized by increasing curvature amplitude along the flagellum generate higher swimming speeds [10,14] compared to those with a uniform curvature amplitude [10,15]. The mechanism behind the speed enhancement is the build-up of elastic stress in the fluid at the high curvature, distal end of the flagellum, which enables sperm to 'push off' of the fluid [10]. Kinematic analysis of sperm flagellar motility, i.e. how shape changes over time, is thus essential to understanding function across species and environments.

Organism morphology had been the cornerstone of taxonomy well into the twentieth century [16,17]. Combined with modern phylogenetic analyses [18], morphological comparisons between organisms have played a key role in the development of the theory of evolution [19,20] and provided important insights into the evolutionary relationships among species. However, direct quantitative links between genotypes and morphological phenotypes [21,22] have been demonstrated only recently, through the use of quantitative morphometric analyses. This approach revealed, for example, that the beak shapes of Darwin's ground finches (*Geospiza*) are shape-invariant upon scale transformations within established phylogenetic groups [21,23], and that the wing shapes in *Drosophila* show similar morphological clades [22] that closely reflect genetic relatedness. In closely related primates (guenons), the analysis of morphological relationships among facial appearances showed that the distinction of conspecifics has driven the evolution of visually discernable facial patterns to maintain diversity for sympatric species [24]. In all of these studies, form served as a surrogate trait for function, to link organism genetics to evolutionary pressures. When organisms—or single cells in the case of spermatozoa—have very similar morphology, shape alone is inadequate to capture differences in functional traits that make organisms specifically suited to their environment.

Shape mode analyses [25] have been applied to morphological studies of organism shape [24,25], and recently have been instrumental in elucidating the locomotion of organisms ranging from multicellular [26] down to single-cell [27] scales. In the context of organism motility, the goal of shape mode analysis is to simplify complex body kinematics, which can instead be quantitatively described by a series of stereotypic postures whose weighting change continuously in time [25]. This approach has been particularly useful in describing the undulatory motion of flatworms (planarians) [26] and eukaryotic flagella [27,28], as well as the peristaltic movement of euglena [29]. For mammalian spermatozoa, modal analysis coupled with high precision tracking has facilitated our understanding of hydrodynamic forces on flagella [27], and it has provided a quantitative understanding of the fluid flows generated by swimming sperm through which they mechanically interact with surfaces and other cells in their surroundings [30]. Comparative flagellar basis mode analysis of swimming cells in response to chemical cues has also yielded key insights into the mechanics of chemotactic turning in human sperm [31].

The recent application of engineering and mathematical approaches to determine relationships among physical traits of organisms has revealed new links between quantifiable phenotypes and organism genotypes [21–24]. These techniques have focused largely on organism shape. In the case of sperm motility and other dynamic processes, however, morphology alone cannot explain differences in those functional traits that make organisms well suited to their environment [9]. Taken as a whole across all species, spermatozoa are regarded as some of the most divergent of all cell types [32], exhibiting exotic shapes [33]. However, a dominant morphology—composed of an approximately 5 µm head and an approximately 50 µm long flagellum with a highly conserved axonemal flagellar structure [2]—is pervasive among the deuterostomes and other organisms (figure 1) [33]. Sperm with this canonical shape, originating from diverse species, move through fluid environments that have widely different rheological and hydrodynamic properties [13,34]. Therefore, we conducted a quantitative comparison among canonically shaped sperm from different species, focusing on swimming kinematics. We use high-speed video microscopy to perform a kinematic analysis of sperm flagellar waveforms and demonstrate that kinematic relatedness correlates more strongly with functional than with genetic relatedness. In particular, we observed that the flagellar waveform kinematics of nine diverse species, spanning chordates and non-chordates, strongly cluster into two distinct groups comprising internal and external fertilizers. Despite the somewhat limited sampling of the vast tree of life, the discordance in waveform kinematics versus organism genetics strongly suggests that the physical environment shapes the evolution of sperm flagellar motility. The novel quantitative approach presented here will help to refine our understanding of the complex landscape of selective pressures that regulate this important link in the reproductive process, and to elucidate key questions surrounding the relative significance of environmental versus genotypic factors in dictating sperm phenotype evolution [9].

2. Methods

2.1. Specimen spawning and media

All sperm samples were prepared with 0.2–0.5% bovine serum albumen to reduce sticking to microfluidic observation chambers. With the exception of human and bull sperm, all sperm samples were held on ice prior to experiments, which were performed at 22°C in filtered artificial sea water. Fertile marine invertebrate (including chordates) parent organisms, including *Arbacia punctulata*, *Lytechinus pictus*, *Lytechinus variegatus*, *Strongylocentrotus purpuratus*, *Ciona intestinalis* and *Haliotis rufescens*, were held in a 15°C artificial seawater (Instant Ocean) aquarium on a 12 h : 12 h light cycle prior to spawning. Sea urchins were spawned by injecting 0.5–1.0 ml of 0.5 M potassium chloride into the body cavity [35], whereas spermatozoa from *C. intestinalis* were collected via dissection [36]. Red abalone (*Ha. rufescens*) were spawned [37] by raising the seawater to pH = 9 for 2.5 h through the addition of 2 M Tris-base and 6% H_2O_2. Sperm were collected by pipette and stored on ice. Zebrafish (*Danio rerio*) sperm was collected from anesthetized, adult, wild-type specimens (strain AB, six months old), by abdominal massage [38] and sperm were held on ice at an osmolarity of 300 mOsm in Hank's balanced salt solution before adjustment to an osmolarity of 150 mOsm to induce motility just prior to experiments. Human sperm samples were obtained from healthy male donors (25–45 years of age) and held at 37°C throughout processing and experiments. Motile sperm were separated from non-motile sperm and white blood cells by the swim-up method [39] in Earle's medium. Bull sperm kinematics were obtained from previously published work [27]. Additional experimental details on the handling and spawning of organisms are found in the electronic supplementary material.

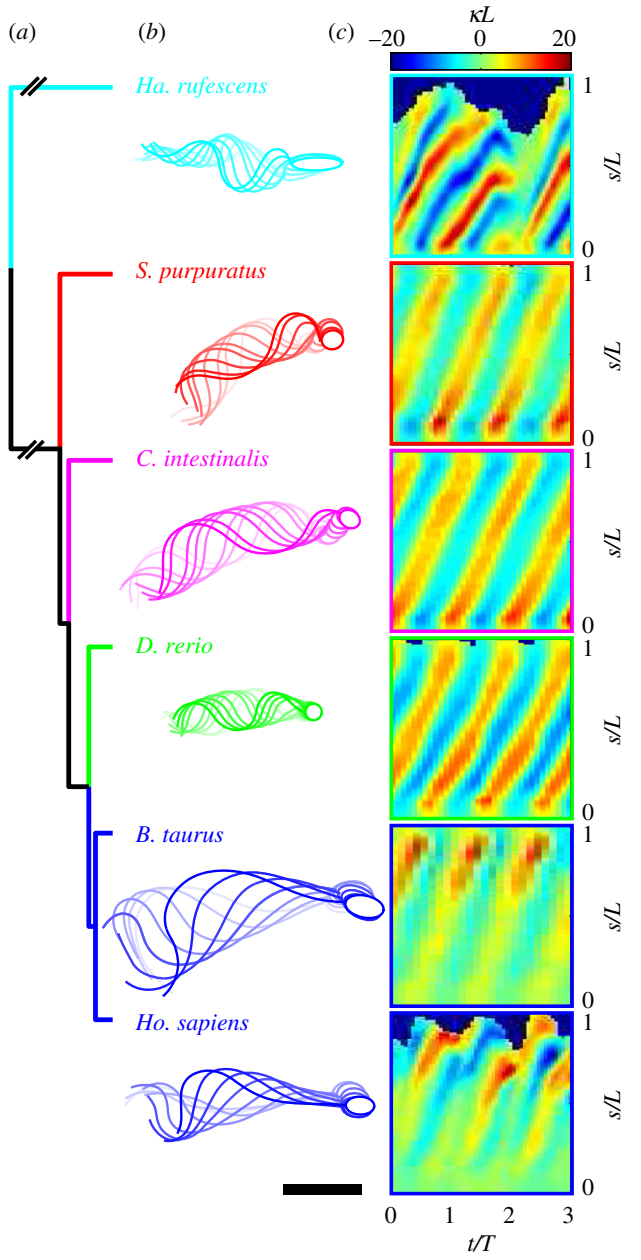

Figure 1. Sperm flagellar waveforms and swimming kinematics characterized by high-speed video microscopy for diverse organisms. (*a*) The phylogenetic relationship among the organisms (spanning internal and external fertilizers, vertebrates and invertebrates) is based on 18 s rRNA sequences (see the electronic supplementary material). (*b*) Flagellar waveforms for sperm cells of select species superimposed over one beat cycle each (see also the electronic supplementary material, figure S1), shown at intervals of one-eighth of the beat period, T. The beat periods and the flagellar lengths were in the range $T = 14$–45 ms and $L = 31$–56 µm, respectively, for all species (electronic supplementary material, table S1). L is taken as the maximum measured projected length for each cell. Scale bar, 15 µm. (*c*) Image analysis reveals the flagellar temporal dynamics through kymographs, representing flagellar curvature, κ (normalized by L), as a function of time, t (normalized by T), and arc length position along the flagellum, s (normalized by L) over three beat cycles each. For cells with slightly three-dimensional waveforms, $s/L < 1$ owing to normalization by the maximum observed flagellar length over the beat cycle, where dark regions represent no data.

2.2. Cell imaging and tracking

Sperm cells were imaged under quiescent fluid conditions using phase contrast microscopy (Nikon Ti-E inverted microscope) in a 120 µm deep, 3 mm wide polydimethylsiloxane microchannel, fabricated through standard soft lithography methods. Flagellar kinematics of sea urchins, *C. intestinalis* and *D. rerio* were captured with a 40× objective (0.6 NA) at 750 frames s^{-1} using a high-speed camera (Photron SA-3, 17 µm $pixel^{-1}$). Flagellar kinematics of abalone (419.5 frames s^{-1}) and human sperm (413 frames s^{-1}) were captured with a 10× objective (0.3 NA) using a high-resolution camera (Andor Neo, 6.5 µm $pixel^{-1}$). Videos were acquired in the cell-accumulated layer within approximately 10 µm of the chamber surfaces, where motile cells tend to collect [40,41] and are generally aligned with the imaging plane. The large microchannel depth (≈10 times larger than the flagellar beat amplitude) ensured that motile cells were not artificially confined. Outside of specialized cases [42], near surface swimming is not definitively known to affect flagellar dynamics. However, all cells were imaged under the same conditions consistent with copious works in the field [2,34], thus enabling comparative studies of cell motility. Additionally, no differences in cell dynamics were observed between the top and bottom of the chamber. Bull sperm kinematics were obtained from 250 frames s^{-1} video [27]. Cell heads and flagella were tracked to sub-pixel accuracy using in-house MATLAB (The Mathworks) routines (see the electronic supplementary material, table S1 for details). Briefly, raw images were background-subtracted, inverted and de-noised using a band-pass filter. Sperm heads and flagella were masked via intensity thresholding, and cell trajectories were constructed through a predictive particle tracking algorithm applied to the intensity weighted head centroids. A 5-point, second-order Savitzky–Golay filter was used to compute the instantaneous cell swimming speed. The flagellar centreline was defined by skeletonization of the flagellar image mask, followed by a Gaussian fit to the image intensity profile normal to the skeleton every 1–4 pixels in arc length. Minor obscured portions of the flagellum were extrapolated using the second- or third-order parametric polynomial fits. Finally, a parametric 5-point, second-order Savitzky–Golay filter was applied to both smooth the segmented flagellum and to compute the local flagellar curvature prior to shape mode analysis (see below). The curvature is defined as $\kappa(s) = (x'y' - y'x')/(x'^2 + y'^2)^{3/2}$, where x and y are the coordinates of the flagellar segment located a distance (arc length), s, along the flagellum measured from head, and primes denote derivatives with respect to s.

2.3. Flagellar waveform analysis

The instantaneous curvature of the flagellum, $\kappa(s)$, was computed for each tracked cell in each video frame as described above. Flagellar waveforms were primarily planar across all species, except for human and abalone sperm, for which the analysis was limited to times when the dominant beating plane (electronic supplementary material) coincided with the imaging plane as determined from the projection of the oblate sperm head (human) and the projected flagellar contour (abalone). In the following description of the analyses, our goal was to extract a set of flagellar curvature basis modes, u_n, whose linear combination best describes the instantaneous flagellar shapes (curvatures) taken on by a selected series of flagellar waveforms from a particular species. As a broad overview of the basis mode decomposition process, selected, instantaneous flagellar curvature vectors were concatenated into a flagellar curvature matrix, M. Flagellar basis modes, u_n, were then determined from the curvature matrix via singular value decomposition (SVD) in MATLAB. SVD is the modal decomposition that underlies common algorithms such as principal component analysis, which has been employed for shape and motility analyses of sperm and other organisms [24–26,28–31]. SVD decomposes these temporal curvature motions exhibited by swimming spermatozoa in M into three components: unitary polynomial basis modes $u_n(s)$, unitary time-dependent modes $V_n(t)$ corresponding to the basis modes, and the magnitude of those

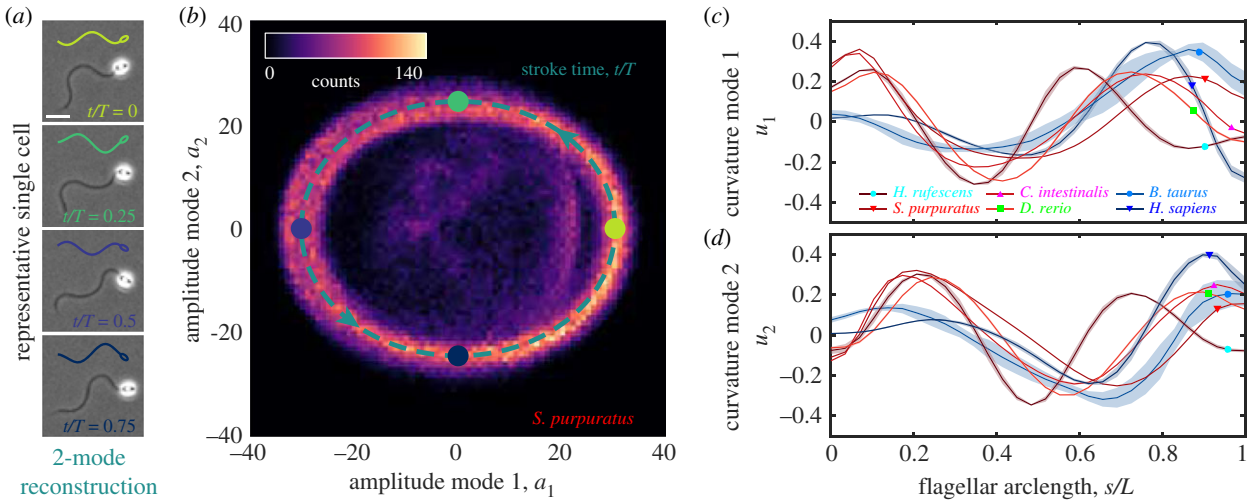

Figure 2. Basis modes of flagellar shape kinematics reveal the 'fingerprint' of flagellar waveforms. (*a*) Flagellar waveform kinematics (lower, *S. purpuratus*) are decomposed from curvature kymographs (figure 1*c*) via SVD into a minimal representation (upper) comprising (*c*,*d*) a set of shape basis modes, $u_n(s)$, and (*b*) corresponding temporal amplitudes, $a_n(t)$. Scale bar, 10 µm. (*b*) A joint histogram of the amplitudes (a_1 and a_2) for the two highest-energy modes (u_1 and u_2) exhibits a cyclic pattern resulting from the highly periodic flagellar beating (*S. purpuratus*). Teal dotted line is the best-fit ellipse, and time points correspond to SVD-informed flagellar shape reconstructions in (*a*). (*c*,*d*) The two highest-energy curvature modes (*c*) $u_1(s)$ and (*d*) $u_2(s)$ are distinct for various species and capture 80–90% of the shape (electronic supplementary material, figures S2 and S3). External fertilizers (red curves; sea urchins, chordate *C. intestinalis*, vertebrate *D. rerio* and protostome *Ha. rufescens*) exhibit strong similarity in their basis modes (see also the electronic supplementary material, figure S2), relative to internal fertilizers (blue curves; *B. taurus* and *Ho. sapiens*). Shaded regions correspond to the local standard deviation of curvature mode, and symbols indicate specific species. Relative errors, computed as the median local standard deviation normalized by the absolute range of each mode, were (2.1, 0.19, 4.8, 0.99, 7.7, 1.4) % for u_1 and (1.9, 0.17, 5.8, 0.95, 7.6, 1.7) % for u_2 for (*Ha. rufescens*, *S. purpuratus*, *C. intestinalis*, *D. rerio*, *B. taurus*, *Ho. sapiens*), respectively.

curvatures at points in time, known as the 'energy', E_n. The energy term is akin to an eigenvalue and the curvature matrix is expressed as $M = uEV^T$. The first two modes ranked by E_n typically represent the predominant shapes of flagella at stroke times offset by $\pi/2$ in a 2π beat cycle. Prior to statistical analyses of flagellar mode shapes, trajectories having mis-tracked sperm flagellar shapes were removed from the dataset by first computing a set of basis modes for each cell track in a given species using SVD. Flagellar waveforms associated with given sperm tracks were retained in the 'species aggregate' data pool if the mean residual flagellar curvature for that cell track satisfied $|\kappa(s,t) - (a_1(t)u_1(s) + a_2(t)u_2(s))|$ less than 0.2 (for external fertilizers) or 0.4 (for internal fertilizers), where $a(t) = EV^T$ is the stroke amplitude.

To determine the principal curvature modes for swimming motion comparison, we applied the SVD analysis to 50 random repartitions of the instantaneously measured flagellar curvatures for the aggregate data pool of each species. This approach enabled us to gain insight into the statistical significance of our analysis, even in the case of a single trajectory (e.g. *B. taurus*). The goal is to find the two defining principal (orthogonal) modes. In general, it is possible that these modes are rotated relative to the principal amplitudes of the flagellar stroke, $a_1(t)$ and $a_2(t)$, where they are given by the maximum and minimum radii of the stroke ellipse (figure 2*b*). To correct for any potential rotation of the modes and produce more accurate flagellar comparison, we adapted a linear algebra-based method of mode rotation for the stroke in basis space [31], which is equivalent to a time shift from the original principal axes at $t = 0$ and $t = \pi/2$. Briefly, a temporal plot of the first two modes of the stroke was fitted by an ellipse (figure 2*b*) and rotated back to its major and minor axes via a rotation matrix (see the electronic supplementary material for details). We note that while degenerate modes are possible, they were not observed in our present analysis, and all strokes had well-defined major and minor axes of the stroke ellipse. The rotation-corrected curvature basis modes, $u_1(s)$ and $u_2(s)$, for the set of 50 data repartitions per species were used for all further analyses, where the mean and standard deviations of the measured modes are shown in figure 2*c*,*d*.

For the purpose of cell basis mode comparison, a kinematic distance metric was developed. The kinematic distance, d, is a dimensionless quantity and defined as the root-mean-square difference (L2-norm) between basis functions of species i and j, which is energy-weighted and averaged over the first two modes ($n = 1,2$) as $d_{i,j} = \Sigma_{n=1,2}\ (E_i^{(n)} + E_j^{(n)})(\langle(u_i^{(n)} - u_j^{(n)})^2\rangle)^{1/2} / \Sigma_{n=1,2}\ (E_i^{(n)} + E_j^{(n)})$ (angled brackets denote an average over the arc length; see the electronic supplementary material). In computing the kinematic distance, d, we allowed for minor dilation and shifting (less than or equal to 10%) of the basis modes along the arc length and scaling of the mode amplitude to find the minimum distance between the two flagellar basis functions [21], which was performed using the 'particleswarm' algorithm in MATLAB (40 points). For two given species i and j, the kinematic distance was computed 50 times for randomly selected (without replacement) basis modes stemming from each of the 50 repartitioned datasets for species i and j. The resulting distance matrix and uncertainty are comprised the median and standard deviation (electronic supplementary material, figure S6), respectively. This approach enabled us to examine both the intra-species (diagonal) and inter-species (off-diagonal) flagellar kinematic distance. We enforced a necessarily symmetric distance matrix by reporting the mean of the forward, $d_{i,j}$, and backward, $d_{j,i}$, kinematic distance values in figure 3*a*.

2.4. Phylogenetic analysis

In order to build a phylogenetic tree of the nine species considered in this study, we obtained ribosomal RNA sequences (electronic supplementary material, table S3) of the 18 s subunit from the Silva database [43]. A consensus sequence was calculated whenever multiple sequences were available for the same species. The genetic distance was calculated for each pair of sequences in order to build the phylogenetic tree (figures 1*a* and 3*c*) using a hierarchical clustering method (unweighted pair group method with arithmetic mean, UPGMA) to cluster sequences based on their similarity. Bootstrapping estimates of the reliability of the results were obtained by carrying out 10^5 replicates of the tree building process.

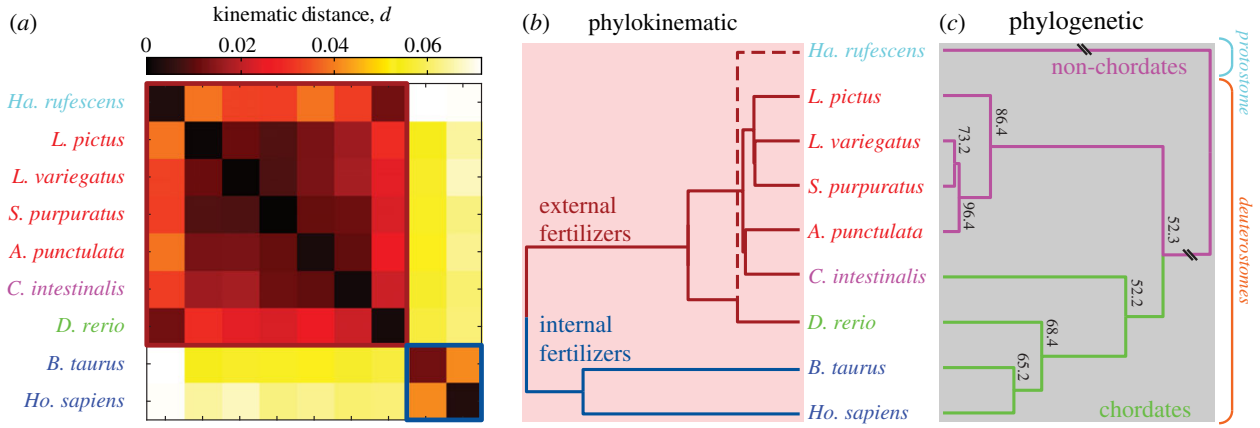

Figure 3. Quantitative comparison of kinematic and genetic relatedness shows that differences in sperm swimming kinematics are not solely determined by phylogenetic relationship. (*a*) The kinematic distance, *d*, quantitatively compares the two highest-energy curvature modes between any two species and is characterized by two distinctly separate islands of similarity, which represent external (red square) and internal (blue square) fertilizers, each having small intra-island kinematic distances between species. (*b*) A phylokinematic tree, based on the sperm cell flagellar kinematics of each species, was constructed directly from the kinematic distance matrix, *d*, where the first bifurcation between external (red branch) and internal (blue branch) fertilizers reflects the islands of similarity in (*a*). (*c*) A phylogenetic tree based on 18 s rRNA sequences illustrates the genetic relationships between the parent organisms, with an early bifurcation that partitions chordates (green branch) and non-chordates (magenta branch). Comparison with the kinematic relatedness (*b*) reveals a starkly different relationship among the organisms. Bootstrapping values are provided at branch bifurcations (see the electronic supplementary material).

3. Results

3.1. Basis mode decomposition quantifies flagellar waveform kinematics

High-speed video microscopy and SVD [24,29,31] were used to quantify and compare the flagellar waveform kinematics of the spermatozoa of nine genetically diverse parent organisms. Supporting movies (electronic supplementary material, movies S1–S9) show swimming spermatozoa of each species. Deuterostomes were the main focus because they encompass important divergences [18] between chordates and non-chordates (figures 1*a* and 3*c*), including four sea urchins (*A. punctulata*, *S. purpuratus*, *L. pictus*, *L. variegatus*), one tunicate (*C. intestinalis*), one fish (*D. rerio*) and two mammals (*B. taurus*, *Ho. sapiens*). One marine invertebrate basal to the deuterostomes, the protostome red abalone (*Ha. rufescens*), was included to root the analysis. These organisms have well-established spawning protocols (see the electronic supplementary material), span the vertebrates and invertebrates, and include external and internal fertilizers. All nine species have canonical sperm morphologies, with 2–10 µm long heads and 30–60 µm long flagella. For each species, microscopy videos were captured for sperm cells collected from one to five parent organisms (electronic supplementary material, table S1). Image analysis yielded the head trajectory and the temporal dynamics of the flagellar shape for each motile spermatozoon in each video (figure 1*b*; electronic supplementary material, figure S1).

The flagellar kinematics of all nine species exhibited the characteristic travelling waves of bending (figure 1*b*) that are responsible for sperm propulsion [1]. The shape dynamics of the flagellum are described by the instantaneous curvature measured in the imaging plane, $\kappa(s,t)$, as a function of flagellar arc length, s, and time, t. The diagonal bands in the curvature kymographs (figure 1*c*; electronic supplementary material, figure S1) signify bending waves propagating down the flagellum. Although rich in information, neither the waveforms nor the kymographs allow a direct, quantitative comparison of flagellar kinematics among species. Likewise, traditional metrics of undulatory propulsion, including wavelength and frequency [15,33,34,44], fail to capture the differential kinematics among species, because they ignore spatial variations in waveform dynamics along the flagellum. We therefore developed a method based on SVD of the flagellar waveforms to obtain metrics in the form of curvature basis modes (see §2.3 and the electronic supplementary material) [24,28,29,31], which enable a detailed, quantitative comparison of swimming kinematics. Considering all time points during the flagellar stroke (figure 2*a*), SVD decomposes the observed flagellar curvature (figure 1*c*), $\kappa(s,t) \approx \Sigma\, a_n(t)u_n(s)$, into a set of time-independent curvature basis modes, $u_n(s)$, with mode number n, each having a time-dependent stroke amplitude, $a_n(t)$ (figure 2*b*). The two highest-energy curvature modes for each species, u_1 and u_2, represent the dominant temporal variation in flagellar curvature among all spermatozoa imaged for that species (figure 2*c*,*d*; electronic supplementary material, figure S2), and generally correspond to curvature modes out of phase by a quarter-cycle. Owing to the periodic flagellar beating, the mode amplitudes are likewise periodic, and thus the first two modes, a_1 and a_2, form a closed cycle [28,31] over time in parametric space (figure 2*b*). The first two curvature modes accounted for 80–90% of the flagellar waveform in each of the nine species (electronic supplementary material, figures S2 and S3 and table S1). This result is corroborated by a reconstruction of the flagellar waveform from the two highest energy, extracted basis modes, which accurately captures the flagellar shape throughout the beat cycle (figure 2*a*). Taken together, the curvature basis modes provide a robust framework for the quantitative comparison of swimming kinematics.

3.2. Kinematic distance reveals two distinct flagellar waveforms among sperm from diverse species

Flagellar kinematics were compared between pairs of species by computing the kinematic distance, d, between the two dominant basis modes found from entire species datasets. Repeating this calculation for all pairs of species yielded a kinematic distance matrix (figure 3*a*). The mean intra-species distance $d = 0.0029$

is the diagonal of the distance matrix and provides a relative measure of similarity among sperm from the same species. In comparison, this self-consistent intra-species distance is one order of magnitude smaller than the mean inter-species distance (off-diagonal elements) among all species examined here ($d = 0.037$) and is an indicator of the significance of our results (see also the electronic supplementary material). Furthermore, the standard deviations of the kinematic distance were universally below ±0.007 with average off-diagonal standard deviation values of ±0.0012 (electronic supplementary material, figure S6), which is significantly below the typical inter-species kinematic distances. Two islands of similarity, each having consistently small intra-island distances, emerged from the kinematic distance matrix (figure 3*a*, dark regions). Each island identifies a group of organisms with similar flagellar kinematics. For example, the flagellar beating modes of the four sea urchin species (figure 2*c*,*d*; electronic supplementary material, figure S2) show strong similarity to one another, with a mean kinematic distance between species of $d = 0.011$ (figure 3*a*) compared to the mean inter-species distance. The basis modes for the two mammalian vertebrates, *Ho. sapiens* and *B. taurus*, also exhibited similarity to one another (figure 2*c*,*d*, blue curves), with $d = 0.041$. The chordate *C. intestinalis*—despite being genetically closer to mammals than to the other tested marine invertebrates [18] (figures 1*a* and 3*c*)—exhibited basis modes considerably closer to the sea urchins ($d = 0.010$–0.018) than to the mammals ($d = 0.056$–0.061). This unexpected similarity indicates that kinematic phenotypes do not necessarily correlate with genetic relatedness.

The two islands of similarity in the kinematic distance matrix (figure 3*a*) correspond to internal fertilizers (blue) and external fertilizers (red), respectively. This result reveals a substantial difference in the flagellar beating patterns of these two groups. The separation between the two islands reflects the mean kinematic distance between the internal and external fertilizers, $d = 0.061$, which exceeds the mean kinematic distance both within internal fertilizers ($d = 0.041$) and within external fertilizers ($d = 0.021$). One island of similarity includes the internal fertilizers *B. taurus* and *Ho. sapiens*. Here, sperm motility, as well as sperm–egg fusion, occurs inside the female reproductive organs. These internal fertilizers exhibit waveforms with considerably lower curvature in the basal region of the flagellum (nearest to the cell head). For example, the maximum curvature mode amplitude (maximum of the absolute value of the curvature averaged over the first two modes for all species) is 61% smaller for internal fertilizers compared to external fertilizers in the first 30% of the flagellum, versus 62% larger in the distal 30% (figure 2*c*,*d*). The other island of similarity comprises the six marine invertebrates (*Ha. rufescens*, four sea urchins, and *C. intestinalis*) and the vertebrate *D. rerio*, which are all external fertilizers, releasing sperm and egg into an aqueous environment. The high curvature in the basal region of the flagellum of external fertilizers results in bending waves that retain nearly constant amplitude as they propagate down the flagellum (figure 1*b*,*c*).

3.3. Flagellar waveform patterns of sperm correlate with fluid environment rather than genetic relatedness

The discordance between kinematic relatedness and genetic relatedness is revealed by the comparison of a newly introduced 'phylokinematic' tree (figure 3*b*) with the phylogenetic tree (figure 3*c*). The latter was constructed based on known 18 s rRNA sequences of the nine organisms (electronic supplementary material, table S3). The relationship among organisms based on the swimming kinematics of their spermatozoa is represented by the phylokinematic tree (figure 3*b*). This tree was constructed in a manner analogous to the phylogenetic tree but using kinematic distance (figure 3*a*) as the similarity metric. In the phylogenetic tree (figure 3*c*) the earliest bifurcation of the deuterostomes separates non-chordates (upper, magenta branch) from chordates [18] (lower, green branch). The phylokinematic tree (figure 3*b*) shares only 33% of this node structure ($p = 0.03$; Robinson–Foulds metric [45]). The earliest bifurcation in the phylokinematic tree segregates external (upper, red branch) from internal (lower, blue branch) fertilizers examined in our study, where such a clustering pattern is extremely unlikely to emerge for randomly generated trees ($p = 0.005$; electronic supplementary material). This dissimilarity between the two trees is primarily owing to the vertebrate *D. rerio* and the chordate *C. intestinalis* sharing more similar waveforms with the non-chordate marine species than with their closer genetic relatives, *B. taurus* and *Ho. sapiens*.

The low curvature observed in the basal region of the flagellum of internal fertilizers (figures 1 and 2) probably stems from mechanically stiff structures on the periphery of the flagellum of these sperm cells [2]. The axoneme, a structure consisting of two sets of dynein motors connecting nine pairs of microtubules (9 + 2) [46], is responsible for the bending of sperm flagella in most species [33]. The highly conserved nature of the axoneme rules this structure out as the cause of the observed waveform variation between internal and external fertilizers. A phylogenetic analysis of dynein motor proteins (figure 4; electronic supplementary material, table S4) reflects the species relatedness obtained from 18 s rRNA sequences (figure 3*c*), supporting this conclusion. Structurally, however, internal-fertilizing cells exhibit an elongated midpiece, outer dense fibres, and a fibrous sheath around the axoneme [2]. The existence of these ultrastructures in mammals

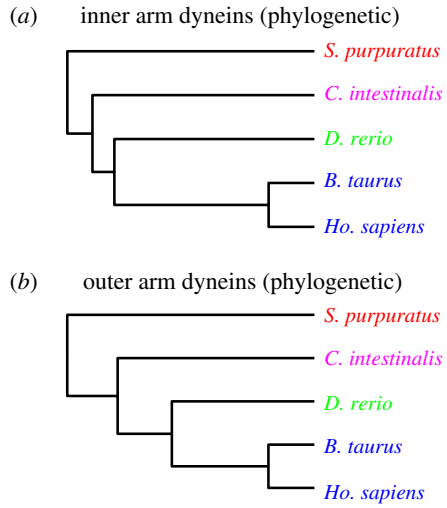

Figure 4. Phylogenetic analysis of axoneme dynein proteins reflects parent organism taxonomy. A comparison of phylogenetic trees based on proteins of both the (*a*) inner and (*b*) outer dynein arms found within the axoneme of the eukaryotic flagellum of the sperm. Inner and outer dyneins are known to affect the flagellar beat frequency and waveform, respectively. However, their phylogenetic trees show no discernable structural differences from the accepted taxonomy of parent organisms based on 18 s rRNA analyses.

and other vertebrates has been well known for many years [2,47], and they confer increased basal bending stiffness [48] that is lacking in external fertilizers. Analysis of flagellar proteins has shown that the protein components of these accessory structures are still detectable in invertebrate sperm, yet the flagellar ultrastructures are not observed in invertebrates [47]. We speculate that the increased basal stiffness is responsible for the low basal flagellar curvature [11], and consequently, for the kinematic segregation between the flagellar waveforms of sperm from the internal and external fertilizers studied here.

3.4. The hydrodynamic environment exerts strong selective pressure on flagellar waveform evolution

The sharp phylokinematic divide between the two islands of similarity in flagellar kinematics (figure 3*a*,*b*) implicates the physical environment as a strong selective pressure [9], driving the evolution of flagellar waveform patterns. In particular, we hypothesize that the observed divide stems from evolution [9] of external fertilizers in Newtonian, low viscosity aquatic environments compared to internal fertilizers in viscous and viscoelastic swimming environments [2,10]. In watery environments, our high-speed imaging experiments (figure 1*b*,*c*; electronic supplementary material, figure S1) confirm the largely uniform flagellar beating amplitude and curvature previously observed in external fertilizers [49], which is predicted to optimize their swimming efficiency [12]. Human sperm and the sperm of other internal fertilizers are often studied in water-like environments not only because of the wide range of potential rheologies experienced by these cells [34], but also for convenience in motility screening assays [2]. Our empirical observations (figure 1*b*,*c*) show that the two internal fertilizers studied here exhibit low basal and high distal waveform curvature when exposed to watery environments, which are highly consistent with prior experiments and theory [34].

Artificially enhanced ambient fluid viscosity has provided valuable insights into flagellar mechanics [34,49,50], and for the sperm of internal fertilizers, it can provide realistic environmental conditions, relative to the range of potential rheologies experienced by these cells [2,34]. To directly determine the mechanical effect of elevated viscosity and viscoelasticity on sperm flagellar kinematics [15,51] in the context of our phylokinematic analysis, we examined human sperm swimming in a medium with properties similar to the upper limit of viscosity of human cervical fluid by following the approach of Smith *et al*. [34]. In high viscosity conditions, the measured waveform (figure 5; electronic supplementary material, movie S10) exhibits a smaller wave propagation speed (electronic supplementary material, table S1), smaller beat amplitude and smaller wavelength as well as reduced three-dimensionality of the flagellar beat compared to low viscosity conditions. These results are in excellent agreement with previous experiments and were independently verified by comparison with high-speed flagellar waveforms extracted from published videos [34]. Elevated viscosity increases the peak flagellar curvature, κ, by a factor of 2–3 (figure 5), and the observed shorter flagellar beat wavelength is evident in the basis modes resulting from the SVD analysis (electronic supplementary material, figure S4). The normalized cumulative energy of these two highest energy modes is also comparable to all other sperm tested (electronic supplementary material, figure S4).

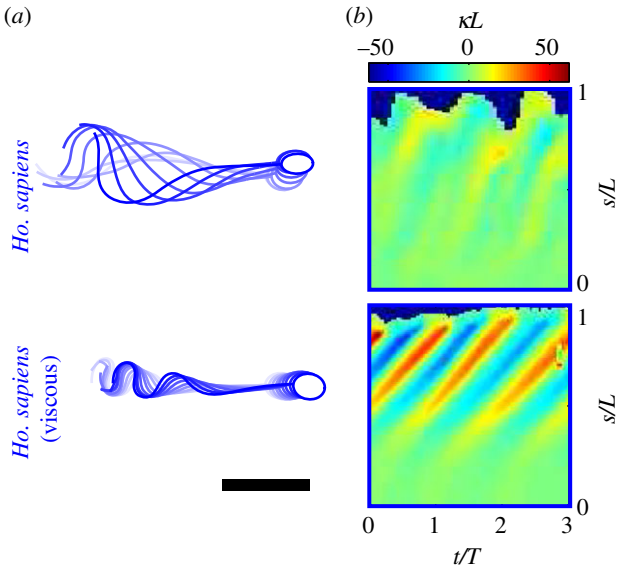

Figure 5. Effects of increased viscosity on human sperm motility. (*a*) Human sperm flagellar motility in water-like conditions (upper, repeated from figure 1) exhibit a notably larger beating amplitude, when compared to swimming in viscous media (lower, 200 cP methylcellulose). Scale bar, 15 µm. (*b*) The corresponding waveform curvature maps show that the reduction in flagellar beat amplitude is accompanied by an increase in the curvature amplitude as well as changes in the propagation of bending waves down the flagellum, in agreement with prior observations [34].

In stark contrast to the enhanced distal flagellar curvature of human sperm in elevated viscosities [34,51], the sperm of external fertilizers—including sea urchin, the tunicate *Ciona* and the annelid *Chaetopterus*—are known to exhibit either uniformly enhanced curvature amplitude or a mildly enhanced proximal flagellar curvature in augmented viscosity environments [49,50]. Thus, elevated ambient viscosity alone does not resolve the fundamental differences in flagellar beat kinematics among external and internal fertilizers, and suggests that the phylokinematic divergence should be maintained under augmented viscosity conditions. We compared the measured waveform modes for human sperm under elevated viscosity conditions to all other assayed sperm. The kinematic distance (electronic supplementary material, figure S5) shows that the induced changes in the flagellar waveform maintain the phylokinematic dissimilarity of the human sperm in a viscous environment relative to the external fertilizers (figure 1; electronic supplementary material, figure S4). The robust, fundamental divide between internal and external fertilizer flagellar kinematics described here is corroborated by recent numerical simulations, which suggest that accessory structures on the flagella of internal fertilizers prevent buckling and enhance motility in elevated viscosity environments [11]. Taken together, our results emphasize that flagellar waveforms are 'hard-wired' into each sperm species through the evolution of flagellar structure and material properties [2], rather than the result of simple viscous, mechanical interactions with the fluid environment alone.

4. Discussion and perspective

In addition to the mechanical properties of the fluid, confinement and ambient fluid flows are two additional, physical features distinguishing the environments of internal and

external fertilizers. By contrast to the spermatozoa of external fertilizers, which mostly swim in unbounded environments, the spermatozoa of internal fertilizers navigate the complex topography of the female reproductive tract, characterized by intricate, corrugated surfaces [52] and micro-porous networks of cervical mucus [53]. For internal-fertilizing insects [52], the complex topography of the reproductive tract is known to influence the evolution of sperm morphology, and convergent evolution of sperm morphology has been observed through coevolution with copulatory organs in flatworms (*Macrostomum*) [54]. Ambient fluid shear also differs considerably for internal and external fertilizers, and shear is known to impact the fertilization process for a wide variety of organisms [6,55]. Low and steady shear guides the sperm of internal fertilizers to the egg via rheotaxis [56]. Strong and unsteady shear experienced by external fertilizers in the turbulent ocean [6,55] may facilitate sperm encounters with eggs via chemotaxis [6]. The intensity of shear in aquatic habitats is highly variable in space: *Ha. rufescens* and *D. rerio* thrive in relatively quiescent fluid environments [6], whereas sea urchins (and to a lesser degree *C. intestinalis*) are found in habitats with stronger shear. The intensity of fluid shear is generally in line with the phylokinematic relatedness of external fertilizers (figure 3*b*,*c*), suggesting that hydrodynamics might have a deep-seated influence over optimal flagellar kinematics [57].

Despite the relatively narrow scope of our analyses in comparison to the vast diversity among the deuterostomes and throughout the tree of life [32], we have demonstrated that our results robustly classify sperm flagellar kinematics for the species considered here. A range of sperm cell body morphologies [33] and flagellar anatomies exist including helical ultrastructure in avian species [58] and alternate microtubule arrangements (9 + 0) among the axonemes of closely related protostomes [59]. While uniform sampling across a clade is often desirable in genetic and evolutionary studies, our present work is limited in a practical way to nine species of spermatozoa comprising model laboratory organisms. This restriction stems partly from the intensive experimental and computational nature of the measurements and the need for robust organism handling and reliable, well-defined spawning protocols. Despite the relatively small sample sizes in our current work, we emphasize that a powerful aspect of our approach is the ability to differentiate nuanced kinematics from among sperm with uniform morphology and scale. In the future, we envision expanding the approach presented here to a broader diversity of organisms. Human and bull sperm are representative of the morphology for many mammals, for which we broadly expect our conclusions to hold. By contrast, sperm from many rodent species (i.e. mammals and internal fertilizers) exhibit prominent falciform (sickle- or hook-shaped) heads and abnormally long and thick flagella [2,12,33]. Asymmetrical head shapes influence swimming motility near surfaces, and for rodents, the falciform head may be important for the fertilization process by facilitating cooperative sperm motility [2,60]. However, based on the high degree of kinematic similarity between the genetically diverse *D. rerio* and *Ha. rufescens*, having head aspect ratios of approximately one and five, respectively, we do not expect head shape to strongly influence flagellar kinematics. Rodent flagella are also known to be morphological outliers [12]. For example, the sperm of Chinese hamsters are more than six times the length (≈260 µm) of the average sperm cells studied in the present work [2], which would probably result in increased kinematic distance from other mammalian sperm. Quantifying and comparing the resulting flagellar kinematic differences among genetic clades will further elucidate the range of evolutionary pressures—probably rooted in the physical environment—that select for the morphology and motility of spermatozoa.

The analysis tools developed in this study also enable us to compare flagellar waveforms for sperm of the same species. This naturally raises questions about the cell-to-cell variations as well as inter-donor and intra-donor variations in sperm motility, which are relevant in the context of fertility screening in humans [2] and for understanding competition in an ecological/evolutionary sense [9]. While not the primary objective of the present study, our limited dataset did enable preliminary insights into flagellar waveform variations within a species. Analysis of flagellar waveforms among individual cells (trajectories) revealed a small median kinematic distance to the species aggregate ($d = 0.0093$; see the electronic supplementary material, figure S7), for example, relative to the mean inter-species distance reported above ($d = 0.037$; figure 3*a*). We also examined the kinematic distance among donors for those species having multiple parent organisms to gauge the potential for donor-to-donor flagellar waveform variability (electronic supplementary material, table S2). The median of the kinematic distance distributions between individual donors and the species aggregate was found to be small ($d < 0.01$) compared to the much larger mean inter-species distances, but in almost all cases statistically significant (i.e. $p < 0.05$, Mann–Whitney U-test). The relatively small kinematic distances among donors suggest that the primary structure of the phylokinematic tree is not affected by donor-to-donor variability. Notably, combined with small p-values from sufficient video microscopy data, these promising results suggest the potential to discern minute differences among sperm populations from the same species for a range of future applications.

Ambient chemical gradients and the physiological state of sperm are known to induce changes in flagellar waveforms including chemotactic motility across species [35] and hyperactivation in human sperm [61], respectively. Similar basis mode analyses to those presented here have yielded key insights into chemotactic turning [31]. In evolving to navigate three-dimensional environments, it is unsurprising that many flagellar waveforms—including those in this study—have some degree of three-dimensionality [62], for example helicoid beat patterns resulting in rolling of the cell body [34]. The sperm studied here had predominantly planar waveforms, which we measured via their two-dimensional projection in the image plane and subsequently removed cell rolling artefacts (electronic supplementary material). While they do not provide a strictly comprehensive viewpoint, we found that two-dimensional waveforms and their basis modes comprise the bulk of sperm waveform information and were sufficient to glean significant conclusions about inter-species flagellar kinematics, similar to copious prior experimental and simulation studies. This point is emphasized by the kinematic similarity between human and bull sperm, where the latter was not observed to roll. Furthermore, only recently have robust three-dimensional flagellar imaging techniques become available [63,64], but these approaches are experimentally complex, computationally intensive, and/or not sufficiently high throughput. Our basis mode analysis is generalizable to higher dimensions. Thus, we envision that the

phylokinematic framework described here will be applied to three-dimensional imaging techniques as they become more widely available, providing yet richer insight into the diversity of flagellar kinematics and other types of cell motility [65] across species.

The identification of kinematic basis modes (figure 2) facilitated the development of a quantitative approach to compare kinematic relatedness across species (figure 3). Fundamental divergences observed in the flagellar kinematics of internal and external fertilizers correlate with differences in the fluid properties and the presence of flagellar ultrastructures, suggesting that the hydrodynamic environment probably exerts strong selective pressure on flagellar waveform evolution of the species considered here. This methodology can have broad applications in medical and engineering processes in which flagellar or ciliary propulsion affects system performance. For example, kinematic analysis promises to provide a deeper physical understanding and potentially more robust diagnoses for ciliopathies [66,67]. Here, subtle changes in flagellar beating cause severe deficiencies in physiological function; including abnormalities in sperm flagella that reduce swimming efficiency and cause infertility [39], and inhibited ciliary function in the lungs owing to increases in mucus viscosity from cystic fibrosis [68]. Likewise, better quantification of the flagellar kinematics in healthy spermatozoa could enable the design of propulsion systems for biomimetic devices, including artificial ciliated surfaces for microscale pumping [69] and swimming microrobots for drug delivery [70]. Understanding flagellar waveforms in real organisms, as optimized through evolution, will help inspire and optimize such engineering solutions.

Ethics. Human sperm samples were obtained under approval by Massachusetts Institute of Technology IRB (COUHES) no. 1012004241.

Data accessibility. Relevant data are available through the Harvard Dataverse at https://doi.org/10.7910/DVN/CPAPV1.

Authors' contributions. J.S.G., J.B.E., F.M., L.J.B., M.P., C.F., A.E.H., R.K.Z. and R.S. designed the research and wrote the paper. J.S.G. performed the experiments. J.S.G., J.B.E., F.M., L.J.B. and M.P. analysed the flagellar waveform data, and F.M. and J.S.G. performed the phylogenetic analysis.

Competing interests. The authors declare no competing interests.

Funding. This work was supported by NSF grant nos. IOS-1120200 (to R.S. and R.K.Z.), IOS-0829643 and OCE-0852361 (to R.K.Z.), OCE-0744641-CAREER and CBET-0966000 (to R.S.), CAREER-1554095 and CBET-1701392 (to J.S.G.); by the UCLA Council on Research (to R.K.Z.); and by a Gordon and Betty Moore Marine Microbial Initiative Investigator Award (no. 3783 to R.S.).

Acknowledgements. We thank Y. Lagadeuc, B. Thomases, A. Morozov and P. Arratia for stimulating discussions, C.A. Zimmer for valuable comments on early drafts of this manuscript, and A. Amsterdam and O. Paugois for assistance with zebrafish sperm sampling.

References

1. Gray J, Hancock GJ. 1955 The propulsion of sea-urchin spermatozoa. *J. Exp. Biol.* **32**, 802–815.
2. Gaffney EA, Gadêlha H, Smith DJ, Blake JR, Kirkman-Brown JC. 2011 Mammalian sperm motility: observation and theory. *Annu. Rev. Fluid Mech.* **43**, 501–528. (doi:10.1146/annurev-fluid-121108-145442)
3. Kaupp UB, Kashikar ND. 2008 Mechanisms of sperm chemotaxis. *Annu. Rev. Physiol.* **70**, 93–117. (doi:10.1146/annurev.physiol.70.113006.100654)
4. Eisenbach M, Giojalas LC. 2006 Sperm guidance in mammals: an unpaved road to the egg. *Nat. Rev. Mol. Cell Biol.* **7**, 276–285. (doi:10.1038/nrm1893)
5. Fisher HS, Hoekstra HE. 2010 Competition drives cooperation among closely related sperm of deer mice. *Nature* **463**, 801–803. (doi:10.1038/nature08736)
6. Zimmer RK, Riffell JA. 2011 Sperm chemotaxis, fluid shear, and the evolution of sexual reproduction. *Proc. Natl Acad. Sci. USA* **108**, 13 200–13 205. (doi:10.1073/pnas.1018666108)
7. Jikeli JF *et al.* 2015 Sperm navigation along helical paths in 3D chemoattractant landscapes. *Nat. Commun.* **6**, 7985. (doi:10.1038/ncomms8985)
8. Brokaw CJ. 1974 Calcium and flagellar response during the chemotaxis of bracken spermatozoids. *J. Cell. Physiol.* **83**, 151–158. (doi:10.1002/jcp.1040830118)
9. Reinhardt K, Dobler R, Abbott J. 2015 An ecology of sperm: sperm diversification by natural selection. *Annu. Rev. Ecol. Evol. Syst.* **46**, 435–459. (doi:10.1146/annurev-ecolsys-120213-091611)
10. Thomases B, Guy RD. 2014 Mechanisms of elastic enhancement and hindrance for finite-length undulatory swimmers in viscoelastic fluids. *Phys. Rev. Lett.* **113**, 098102. (doi:10.1103/PhysRevLett.113.098102)
11. Gadêlha H, Gaffney EA. 2019 Flagellar ultrastructure suppresses buckling instabilities and enables mammalian sperm navigation in high-viscosity media. *J. R. Soc. Interface* **16**, 20180668. (doi:10.1098/rsif.2018.0668)
12. Tam D, Hosoi AE. 2011 Optimal kinematics and morphologies for spermatozoa. *Phys. Rev. E* **83**, 045303. (doi:10.1103/PhysRevE.83.045303)
13. Critchfield AS, Yao G, Jaishankar A, Friedlander RS, Lieleg O, Doyle PS, McKinley G, House M, Ribbeck K. 2013 Cervical mucus properties stratify risk for preterm birth. *PLoS ONE* **8**, e69528. (doi:10.1371/journal.pone.0069528)
14. Teran J, Fauci L, Shelley M. 2010 Viscoelastic fluid response can increase the speed and efficiency of a free swimmer. *Phys. Rev. Lett.* **104**, 038101. (doi:10.1103/PhysRevLett.104.038101)
15. Shen XN, Arratia PE. 2011 Undulatory swimming in viscoelastic fluids. *Phys. Rev. Lett.* **106**, 1–4. (doi:10.1103/PhysRevLett.106.208101)
16. Thompson DW. 1992 *On growth and form*, 2nd edn. Cambridge, UK: Cambridge University Press.
17. Arthur W. 2006 D'Arcy Thompson and the theory of transformations. *Nat. Rev. Genet.* **7**, 401–406. (doi:10.1038/nrg1835)
18. Delsuc F, Brinkmann H, Chourrout D, Philippe H. 2006 Tunicates and not cephalochordates are the closest living relatives of vertebrates. *Nature* **439**, 965–968. (doi:10.1038/nature04336)
19. Darwin C. 1860 *On the origin of species by means of natural selection, or the preservation of favored races in the struggle for life*. New York, NY: D. Appleton and Company.
20. Leibold MA. 1995 The niche concept revisited: mechanistic models and community context. *Ecology* **76**, 1371–1382. (doi:10.2307/1938141)
21. Campàs O, Mallarino R, Herrel A, Abzhanov A, Brenner MP. 2010 Scaling and shear transformations capture beak shape variation in Darwin's finches. *Proc. Natl Acad. Sci. USA* **107**, 3356–3360. (doi:10.1073/pnas.0911575107)
22. Jones GW, Mahadevan L. 2013 Planar morphometry, shear and optimal quasi-conformal mappings. *Proc. R. Soc. A* **469**, 20120653. (doi:10.1098/rspa.2012.0653)
23. Mallarino R, Campas O, Fritz JA, Burns KJ, Weeks OG, Brenner MP, Abzhanov A. 2012 Closely related bird species demonstrate flexibility between beak morphology and underlying developmental programs. *Proc. Natl Acad. Sci. USA* **109**, 16 222–16 227. (doi:10.1073/pnas.1206205109)
24. Allen WL, Stevens M, Higham JP. 2014 Character displacement of Cercopithecini primate visual signals. *Nat. Commun.* **5**, 4266. (doi:10.1038/ncomms5266)
25. Werner S, Rink JC, Riedel-Kruse IH, Friedrich BM. 2014 Shape mode analysis exposes movement patterns in biology: flagella and flatworms as case studies. *PLoS ONE* **9**, e0113083. (doi:10.1371/journal.pone.0113083)

26. Stephens GJ, Johnson-Kerner B, Bialek W, Ryu WS. 2008 Dimensionality and dynamics in the behavior of *C. elegans*. *PLoS Comput. Biol.* **4**, e1000028. (doi:10.1371/journal.pcbi.1000028)
27. Friedrich BM, Riedel-Kruse IH, Howard J, Jülicher F. 2010 High-precision tracking of sperm swimming fine structure provides strong test of resistive force theory. *J. Exp. Biol.* **213**, 1226–1234. (doi:10.1242/jeb.039800)
28. Battle C, Broedersz CP, Fakhri N, Geyer VF, Howard J, Schmidt CF, MacKintosh FC. 2016 Broken detailed balance at mesoscopic scales in active biological systems. *Science* **352**, 604–607. (doi:10.1126/science.aac8167)
29. Arroyo M, Heltai L, Millán D, DeSimone A. 2012 Reverse engineering the euglenoid movement. *Proc. Natl Acad. Sci. USA* **109**, 17 874–17 8749. (doi:10.1073/pnas.1213977109)
30. Ishimoto K, Gadêlha H, Gaffney EA, Smith DJ, Kirkman-Brown J. 2017 Coarse-graining the fluid flow around a human sperm. *Phys. Rev. Lett.* **118**, 1–5. (doi:10.1103/PhysRevLett.118.124501)
31. Saggiorato G, Alvarez L, Jikeli JF, Kaupp UB, Gompper G, Elgeti J. 2017 Human sperm steer with second harmonics of the flagellar beat. *Nat. Commun.* **8**, 1415. (doi:10.1038/s41467-017-01462-y)
32. Pitnick S, Hosken DJ, Birkhead TR. 2009 *Sperm morphological diversity*, 1st edn. Amsterdam, The Netherlands: Elsevier.
33. Brennen C, Winet H. 1977 Fluid mechanics of propulsion by cilia and flagella. *Annu. Rev. Fluid Mech.* **9**, 339–398. (doi:10.1146/annurev.fl.09.010177.002011)
34. Smith DJ, Gaffney EA, Gadelha H, Kapur N, Kirkman-Brown JC. 2009 Bend propagation in the flagella of migrating human sperm, and its modulation by viscosity. *Cell* **66**, 220–236. (doi:10.1002/cm.20345)
35. Alvarez L, Dai L, Friedrich BM, Kashikar ND, Gregor I, Pascal R, Kaupp UB. 2012 The rate of change in $Ca2^+$ concentration controls sperm chemotaxis. *J. Cell Biol.* **196**, 653–663. (doi:10.1083/jcb.201106096)
36. Veeman MT, Chiba S, Smith WC. 2011 *Ciona* genetics. *Methods Mol. Biol.* **770**, 401–422. (doi:10.1007/978-1-61779-210-6)
37. Riffell JA, Zimmer RK. 2007 Sex and flow: the consequences of fluid shear for sperm–egg interactions. *J. Exp. Biol.* **210**, 3644–3660. (doi:10.1242/jeb.008516)
38. Jing R, Huang C, Bai C, Tanguay R, Dong Q. 2009 Optimization of activation, collection, dilution, and storage methods for zebrafish sperm. *Aquaculture* **290**, 165–171. (doi:10.1016/j.aquaculture.2009.02.027)
39. Cooper TG *et al.* 2009 World Health Organization reference values for human semen characteristics. *Hum. Reprod. Update* **16**, 231–245. (doi:10.1093/humupd/dmp048)
40. Rothschild L. 1963 Non-random distribution of bull spermatozoa in a drop of sperm suspension. *Nature* **198**, 1221–1222. (doi:10.1038/1981221a0)
41. Elgeti J, Kaupp UB, Gompper G. 2010 Hydrodynamics of sperm cells near surfaces. *Biophys. J.* **99**, 1018–1026. (doi:10.1016/j.bpj.2010.05.015)
42. Nosrati R, Driouchi A, Yip CM, Sinton D. 2015 Two-dimensional slither swimming of sperm within a micrometre of a surface. *Nat. Commun.* **6**, 8703. (doi:10.1038/ncomms9703)
43. Quast C, Pruesse E, Yilmaz P, Gerken J, Schweer T, Yarza P, Peplies J, Glöckner FO. 2013 The SILVA ribosomal RNA gene database project: improved data processing and web-based tools. *Nucleic Acids Res.* **41**, D590–D596. (doi:10.1093/nar/gks1219)
44. Brokaw CJ. 1966 Effects of increased viscosity on the movements of some invertebrate spermatozoa. *J. Exp. Biol.* **45**, 113–139.
45. Robinson DR, Foulds LR. 1981 Comparison of phylogenetic trees. *Math. Biosci.* **53**, 131–147. (doi:10.1016/0025-5564(81)90043-2)
46. King S. 2012 *Dyneins: structure, biology and disease*. Waltham, MA: Elsevier Inc.
47. Inaba K. 2011 Sperm flagella: comparative and phylogenetic perspectives of protein components. *Mol. Hum. Reprod.* **17**, 524–538. (doi:10.1093/molehr/gar034)
48. Lindemann CB. 1996 Functional significance of the outer dense fibers of mammalian sperm examined by computer simulations with the geometric clutch model. *Cell Motil. Cytoskeleton* **34**, 258–270. (doi:10.1002/(sici)1097-0169(1996)34:4<258::aid-cm1>3.0.co;2-4)
49. Woolley DM, Vernon GG. 2001 A study of the helical and planar waves on sea urchin sperm flagella, with a theory of how they are generated. *J. Exp. Biol.* **204**, 1333–1345.
50. Brokaw CJ. 1966 Effects of increased viscosity on the movements of some invertebrate spermatozoa. *J. Exp. Biol.* **45**, 113–139.
51. Ishijima S, Oshio S, Mohri H. 1986 Flagellar movement of human spermatozoa. *Gamete Res.* **13**, 185–197. (doi:10.1002/mrd.1120130302)
52. Higginson DM, Miller KB, Segraves K A, Pitnick S. 2012 Female reproductive tract form drives the evolution of complex sperm morphology. *Proc. Natl Acad. Sci. USA* **109**, 4538–4543. (doi:10.1073/pnas.1111474109)
53. Rutllant J, López-Béjar M, López-Gatius F. 2005 Ultrastructural and rheological properties of bovine vaginal fluid and its relation to sperm motility and fertilization: a review. *Reprod. Domest. Anim.* **40**, 79–86. (doi:10.1111/j.1439-0531.2004.00510.x)
54. Schärer L, Littlewood DTJ, Waeschenbach A, Yoshida W, Vizoso DB. 2011 Mating behavior and the evolution of sperm design. *Proc. Natl Acad. Sci. USA* **108**, 1490–1495. (doi:10.1073/pnas.1013892108)
55. Crimaldi JP, Zimmer RK. 2014 The physics of broadcast spawning in benthic invertebrates. *Ann. Rev. Mar. Sci.* **6**, 141–165. (doi:10.1146/annurev-marine-010213-135119)
56. Kantsler V, Dunkel J, Blayney M, Goldstein RE. 2014 Rheotaxis facilitates upstream navigation of mammalian sperm cells. *Elife* **3**, e02403. (doi:10.7554/eLife.02403)
57. Kumar M, Walkama DM, Guasto JS, Ardekani AM. 2019 Flow-induced buckling dynamics of sperm flagella. *Phys. Rev. E* **100**, 63107. (doi:10.1103/PhysRevE.100.063107)
58. Vernon GG, Woolley DM. 1999 Three-dimensional motion of avian spermatozoa. *Cell Motil. Cytoskeleton* **42**, 149–161. (doi:10.1002/(sici)1097-0169(1999)42:2<149::aid-cm6>3.0.co;2-0)
59. Ishijima S, Sekiguchi K, Hiramoto Y. 1988 Comparative study of the beat patterns of American and Asian horseshoe crab sperm: evidence for a role of the central pair complex in forming planar waveforms in flagella. *Cell Motil. Cytoskeleton* **9**, 264–270. (doi:10.1002/cm.970090308)
60. Immler S, Moore HDM, Breed WG, Birkhead TR. 2007 By hook or by crook? Morphometry, competition and cooperation in rodent sperm. *PLoS ONE* **2**, e0000170. (doi:10.1371/journal.pone.0000170)
61. Spehr M, Gisselmann G, Poplawski A, Riffell JA, Wetzel CH, Zimmer RK, Hatt H. 2003 Identification of a testicular odorant receptor mediating human sperm chemotaxis. *Science* **299**, 2054–2058. (doi:10.1126/science.1080376)
62. Ishijima BYS, Hamaguchi MS, Ishijima SA, Hamaguchi Y. 1992 Rotational movement of a spermatozoon around its long axis. *J. Exp. Biol.* **163**, 15–31.
63. Wilson LG, Carter LM, Reece SE. 2013 High-speed holographic microscopy of malaria parasites reveals ambidextrous flagellar waveforms. *Proc. Natl Acad. Sci. USA* **110**, 18 769–18 774. (doi:10.1073/pnas.1309934110)
64. Rossi M, Cicconofri G, Beran A, Noselli G, DeSimone A. 2017 Kinematics of flagellar swimming in *Euglena gracilis*: helical trajectories and flagellar shapes. *Proc. Natl Acad. Sci. USA* **114**, 13 085–13 090. (doi:10.1073/pnas.1708064114)
65. Stout DA, Bar-Kochba E, Estrada JB, Toyjanova J, Kesari H, Reichner JS, Franck C. 2016 Mean deformation metrics for quantifying 3D cell-matrix interactions without requiring information about matrix material properties. *Proc. Natl Acad. Sci. USA* **113**, 2898–2903. (doi:10.1073/pnas.1510935113)
66. Novarino G, Akizu N, Gleeson JG. 2011 Review modeling human disease in humans: the ciliopathies. *Cell* **147**, 70–79. (doi:10.1016/j.cell.2011.09.014)
67. Inaba K, Mizuno K. 2016 Sperm dysfunction and ciliopathy. *Reprod. Med. Biol.* **15**, 77–94. (doi:10.1007/s12522-015-0225-5)
68. Cheung ATW, Jahn TL. 1976 High speed cinemicrographic studies on rabbit tracheal (ciliated) epithelia: cytolytic effect of cystic fibrosis serum on tracheal epithelial cells. *Pediatr. Res.* **10**, 144–147. (doi:10.1203/00006450-197602000-00015)
69. Vilfan M, Potocnik A, Kavcic B, Osterman N, Poberaj I, Vilfan A, Babic D. 2010 Self-assembled artificial cilia. *Proc. Natl Acad. Sci. USA* **107**, 1844–1847. (doi:10.1073/pnas.0906819106)
70. Nelson BJ, Kaliakatsos IK, Abbott JJ. 2010 Microrobots for minimally invasive medicine. *Annu. Rev. Biomed. Eng.* **12**, 55–85. (doi:10.1146/annurev-bioeng-010510-103409)